Multifunctional Cu_2TSiS_4 (T = Mn and Fe): Polar Semiconducting Antiferromagnets with Nonlinear Optical Property

Zachary T. Messegee,[1] Jeong Bin Cho,[2] Jun Sang Cho,[2] Andrew J. Craig,[3] V. Ovidiu Garlea,[4] Yan Xin,[5] Chang-Jong Kang,[6,7] Thomas E. Proffen,[4] Hari Bhandari,[8,9] Jordan C. Kelly,[3] Nirmal J. Ghimire,[8,9] Jennifer A. Aitken,[3] Joon I. Jang,[*,2] Xiaoyan Tan[*,1]

[1]*Department of Chemistry and Biochemistry, George Mason University, Fairfax, Virginia 22030, United States*
[2]*Department of Physics, Sogang University, Seoul 04017, Republic of Korea*
[3]*Department of Chemistry and Biochemistry, Duquesne University, Pittsburgh, Pennsylvania 15282, United States*
[4]*Neutron Scattering Division, Oak Ridge National Laboratory, Oak Ridge, Tennessee 37831, United States*
[5]*National High Magnetic Field Laboratory, Florida State University, Tallahassee, Florida 32310, United States*
[6]*Department of Physics, Chungnam National University, Daejeon 34134, Republic of Korea*
[7]*Institute of Quantum Systems, Chungnam National University, Daejeon 34134, Republic of Korea*
[8]*Department of Physics and Astronomy, George Mason University, Fairfax, Virginia 22030, United States*
[9]*Quantum Science and Engineering Center, George Mason University, Fairfax, Virginia 22030, United States*

Abstract

Cu_2TSiS_4 (T = Mn and Fe) polycrystalline and single crystal materials were prepared with high-temperature solid-state and chemical vapor transport methods, respectively. The polar crystal structure (space group $Pmn2_1$) consists of chains of corner-sharing and distorted CuS_4, Mn/FeS_4, and SiS_4 tetrahedra, which is confirmed by the Rietveld refinement using neutron powder diffraction data, X-ray single crystal refinement, electron diffraction, energy-dispersive X-ray spectroscopy, and second harmonic generation (SHG) techniques. Magnetic measurements indicate that both compounds order antiferromagnetically at 8 and 14 K, respectively, which is supported by the temperature-dependent (100-2 K) neutron powder diffraction data. Additional magnetic reflections observed at 2 K can be modeled by magnetic propagation vectors k = (½,0,½) and k = (½,½,½) for Cu_2MnSiS_4 and Cu_2FeSiS_4, respectively. The refined antiferromagnetic structure reveals the Mn/Fe spins are canted away from the *ac* plane by about 14°, with the total magnetic moment of Mn and Fe being 4.1(1) and 2.9(1) μ_B, respectively. Both compounds exhibit an SHG response but with relatively modest second-order nonlinear susceptibilities. Density functional theory calculations are used to describe the electronic band structures.

Introduction

$Cu_2T^{II}M^{IV}S_4$ (T = Mn, Fe, Co, Ni, Cu, Zn, Cd, and Hg; M = Si, Ge, and Sn), simplified as CTMS, and related quaternary chalcogenides are important semiconductors that have various optoelectronic and energy-related applications such as nonlinear optics,[1] solar cell technology,[2,3] gamma-ray detectors,[4] supercapacitors,[5] and thermoelectric materials.[6,7,8] CTMS compounds adopt either the tetragonal stannite ($I\bar{4}2m$),[9] tetragonal kesterite ($I\bar{4}$),[10] tetragonal pseudo-cubic ($P\bar{4}$),[11] or orthorhombic wurtz-stannite ($Pmn2_1$) structure type.[12] The most common crystal structure type for CTMS compounds is stannite (St), e.g., Cu_2FeSnS_4, which is a superstructure derived from sphalerite (Sp) such at $a_{St} \sim a_{Sp}$; $c_{St} \sim 2\ a_{Sp}$.[12] The wurtz-stannite (WSt) crystal structure is a superstructure of wurtzite (W) via a doubling of the unit cell along the *a* axis ($a_{WSt} \sim 2\ a_W$; $b_{WSt} \sim \sqrt{3}a_W$; $c_{WSt} \sim c_W$), with the same metal-sulfur coordination environment as in St.[12] While the three tetragonal structure types are nonpolar, WSt possesses a polar crystal structure.

The only CTMS compounds reported thus far with the polar WSt crystal structure are Cu_2MnGeS_4 and Cu_2TSiS_4 (T = Mn and Fe).[12] Polar Cu_2MnGeS_4 has been reported to be highly sensitive to gamma-rays and neutrons, as well as a good nonlinear optical (NLO) material exhibiting a strong SHG response at room temperature.[4,1] Cu_2MnGeS_4 adopts a magnetic space group $P_{2a}c$ with antiferromagnetically coupled spins in a collinear arrangement.[13] Similar to Cu_2MnGeS_4, Cu_2TSiS_4 (T = Mn and Fe) caught our attention as intriguing multifunctional magnetic semiconductors containing non-toxic and earth-abundant elements that could potentially be used as photovoltaic, NLO, ferroelectric, magnetoelectric, and multiferroic materials.[14] Understanding the magnetic structure is important for multiferroic materials. Cu_2TSiS_4 (T = Mn and Fe) are reported to adopt the polar WSt structure based on X-ray single crystal (for T = Mn) and powder (for T = Fe) diffraction data, and both compounds are antiferromagnets with Néel temperature (T_N) at 8 and 15 K, respectively.[12,15,16] However, the magnetic structures, optical bandgaps, transparency windows, NLO properties, and definitive confirmation of the polar crystal structures have not yet been investigated.

In this study, we use X-ray powder diffraction (XRPD), neutron powder diffraction (NPD), and transmission electron microscopy (TEM) techniques to confirm the reported polar crystal structure of Cu_2TSiS_4 (T = Mn and Fe). Here, we also report the magnetic properties, magnetic structures, optical bandgaps, optical transparency in the infrared region, and second-order NLO properties of Cu_2TSiS_4 (T = Mn and Fe) by magnetic measurements, temperature-dependent NPD, diffuse reflectance UV-vis spectroscopy, attenuated total reflectance (ATR) Fourier transform infrared (FT-IR) spectroscopy, and second-order NLO property measurements, respectively.

Experimental Section

Starting Materials and Synthesis. Cu_2TSiS_4 (T = Mn and Fe) samples were prepared by heating the mixture of Cu (99.999% mass fraction, Alfa Aesar), Si (99.999% mass fraction, Alfa Aesar), and S (99.5% mass fraction, Alfa Aesar) powders with either Mn (99.95% mass fraction, Alfa Aesar) or Fe (99.99% mass fraction, Alfa Aesar) powders that were thoroughly ground and pressed into a pellet (6 mm in diameter). All sample preparations were carried out inside an argon-filled glove box with an O_2 and H_2O concentration of less than 1 ppm. Each pellet was then loaded in a quartz tube that was sealed under a dynamic vacuum (< 10^{-3} Torr). The obtained ampoule was heated in a box furnace at 600 °C for 1 d and 900 °C for 3 d with the heating and cooling rates of 100 and 150 °C/h, respectively, with a modified heating profile based on the previous report.[12] Single crystals ($< 1 \times 1.5 \times 0.3$ mm^3) of Cu_2TSiS_4 (T = Mn and Fe) were grown via the chemical vapor transport (CVT) method with iodide as the transport agent. For the CVT method, the mixture of elements was heated with a similar heating profile as the solid-state method but with a longer dwelling time (5 d) at 900 °C.

X-ray and Neutron Powder Diffraction. Room-temperature laboratory XRPD patterns for the polycrystalline samples were collected with a scattering angle 2Θ ranging from 10 to 70° for 30 min using a Rigaku Miniflex-600 benchtop X-ray powder diffractometer (Cu K_α, $\lambda = 1.5418$ Å). NPD data were collected for ~3 g of the microcrystalline Cu_2TSiS_4 (T = Mn and Fe) samples using a powder diffractometer POWGEN at the Spallation Neutron Source, Oak Ridge National Laboratory.[17] A neutron band with a center wavelength of 2.67 Å was used to collect the data. NPD data were obtained at various temperatures between 100 and 2 K. Rietveld refinements and data analysis using the NPD data were carried out by employing the suite of FullProf programs.[18] Magnetic structure symmetry analysis was performed with the computational tools at the Bilbao crystallographic server.[19]

X-ray Single Crystal Diffraction. X-ray single crystal diffraction data for Cu_2TSiS_4 (T = Mn and Fe) were obtained at room temperature on a Rigaku XtaLAB Synergy-i diffractometer with a HyPix-Bantam direct photon-counting detector and Mo K_α radiation. Small single crystals were mounted on a loop and measured on the goniometer head of the diffractometer. Data reduction and absorption correction were carried out using the Rigaka CrysAlis^{Pro} package. The crystal structure of Cu_2TSiS_4 (T = Mn and Fe) was solved with the space group $Pmn2_1$ and refined using the SHELX-2018 software.[20] A summary of data collection and refined structure parameters is presented in Table S1. The corresponding atomic positions and anisotropic thermal parameters are provided in Table S2 and S3.

Transmission Electron Microscopy. TEM experiments were conducted with a probe-aberration-corrected sub-Å resolution JEOL JEM-ARM200cF microscope using an accelerating voltage of 200 kV. Polycrystalline Cu_2TSiS_4 (T = Mn and Fe) powders were crushed into thin electron-transparent pieces, which were transferred onto a carbon-coated 200-mesh Cu TEM grid. For the Cu_2FeSiS_4 sample, a few single crystals were also used for preparing thin pieces in a similar way to that which was used for the Cu_2TSiS_4 (T = Mn and Fe) powder samples. Selected area electron diffraction (SAED) patterns were obtained along the [100] or [001] direction on a single crystal piece, and corresponding atomic resolution high-angle-annular-dark-field scanning transmission electron microscopy (HAADF-STEM) images were collected.

Chemical Analysis. Elemental analysis of Cu_2TSiS_4 (T = Mn and Fe) was performed on single crystals with an Octane Elect Plus energy-dispersive X-ray (EDX) spectroscopy system, an accessory of a JEOL JSM-IT500HRLV scanning electron microscope (SEM). The SEM images and elemental maps were collected with an accelerating voltage of 15 kV.

Magnetic Measurements. Cu_2TSiS_4 (T = Mn and Fe) powders were loaded in a plastic capsule inside a plastic straw for the magnetic property measurements with the quantum design DynaCool physical property measurement system. Zero-field-cooled (ZFC) and field-cooled (FC) protocols were used to measure the magnetic susceptibility between 1.8 and 300 K with an applied magnetic field (H) of 0.1 T. Isothermal field-dependent magnetization was measured at 1.8 and 300 K using H ranging ± 9 T.

Attenuated Total Reflectance Fourier Transform Infrared Spectroscopy. Optical transparency data were collected with 256 scans from 400 to 4000 cm^{-1} using a Thermo Nicolet 380 FT-IR spectrometer with an ATR accessory. The OMNIC software was used to collect and analyze the spectra. This method, where a diamond crystal is in optical contact with the samples, results in the thickness-dependent effect on the intensity of the spectra being negligible.[21] This is due to the penetration depth into the sample approaching the lower limit of the particle size, approximately 2 μm, within the sample.

Second-order NLO Property Measurements. Crystalline Cu_2TSiS_4 (T = Mn and Fe) powders were sieved into discrete particle size ranges of < 20 μm, 20–45 μm, 45–75 μm, 75–90 μm, 90–106 μm, 106–125 μm, 125–150 μm, and > 150 μm by employing a collection of stainless steel W.S. Tyler® test sieves and a Gilson sieve shaker in order to investigate the phase-matching (PM) nature of SHG of the samples. Each sample was enclosed in a glass capillary tube by flame sealing under the vacuum to prevent moisture and air exposure to the samples during measurements. The capillary tubes were mounted on a homemade sample holder, and the measured SHG efficiencies of the samples were compared to those of the optical-quality reference materials, $AgGaS_2$ (AGS) and $AgGaSe_2$ (AGSe), for the estimation of the second-order nonlinear susceptibility, $\chi^{(2)}$. Note that the particle size ranges for the AGS and AGSe benchmark materials obtained from G&H Cleveland are a bit dissimilar to those of the samples, but this does not influence our NLO property analysis.

SHG measurements were recorded at room temperature using an input wavelength of λ = 1800 nm. Coherent light with λ = 1064 nm was firstly generated by an EKSPLA PL-2250 series diode-pumped Nd:YAG laser with a pulse width of 30 ps and a repetition rate of 50 Hz to generate tunable pulses. The Nd:YAG laser pumped an EKSPLA Harmonics Unit H400, where the input beam frequency was tripled to 355 nm via a series of NLO beam mixing. Two beams of 355 and 1064 nm next passed into an EKSPLA PG403-SH-DFG Optical Parametric Oscillator consisting of four principle components: (i) a double-pass parametric generator, (ii) a single-pass parametric amplifier, (iii) a second-harmonic generator, and (iv) a difference frequency generation. A full explanation of the laser and detection setup has been provided previously.[22]

Density Functional Theory Calculations. The all-electron, full-potential linearized augmented plane-wave method implemented in WIEN2k was used to calculate the electronic structure.[23] Structural parameters were taken from NPD refinement. The Perdew-Burke-Ernzerhof generalized gradient approximation (GGA) was adopted for the exchange-correlation functional.[24] 14 × 14 × 22 and 16 × 17 × 16 *k* meshes were used in the Brillouin zone integration for Cu_2MnSiS_4 and Cu_2FeSiS_4, respectively. The muffin tin radii were chosen to be 2.37, 2.47, 2.36, 1.83, and 1.93 Bohr radii for Fe, Mn, Cu, Si, and S, respectively, and the size of a plane-wave basis set was determined from $R_{mt}K_{max}$ of 7.0, where R_{mt} is the smallest atomic muffin tin radius, and K_{max} is the largest plane-wave vector. To consider the strong correlation effect, GGA+U was adopted within the fully localized limit.[25,26] The effective on-site Coulomb interaction parameters, $U_{eff} = U - J$, of 4.0 and 5.0 eV were used for Mn-*d* and Fe-*d* orbitals, respectively.

Results and Discussion

Crystal Structure. The XRPD patterns of the polycrystalline Cu_2TSiS_4 (T = Mn and Fe) samples prepared via the high-temperature solid-state synthesis match the theoretical patterns calculated from the polar structure in the space group $Pmn2_1$ (Figure S1). The crystal structure of Cu_2TSiS_4 (T = Mn and Fe) is a cation-ordered, orthorhombic superstructure of the wurtzite structure. The wurtzite (ZnS) structure is built from the hexagonal closest packing of S ions, where the metal ions occupy half of the tetrahedral holes. In this structure, all cations are tetrahedrally coordinated by sulfide anions and vice versa. As shown in the crystal structure of Cu_2MnSiS_4, the CuS_4 tetrahedra are connected via corner-sharing along the crystallographic *a* axis and form CuS_4 columns that are connected in a zigzag fashion along the crystallographic *c* axis (Figure 1a). Similarly, MnS_4 and SiS_4 are mixed alternately to form zigzag layers between the CuS_4 layers along the *b* axis.

The refinements of the crystal structure of Cu_2TSiS_4 (T = Mn and Fe) were carried out using the NPD data collected at 90 and 100 K, respectively. The reported polar crystal structure of Cu_2TSiS_4 (T = Mn and Fe) in space group $Pmn2_1$ was used as the initial model during the Rietveld refinements. However, it became apparent that a relatively small amount of other phases were detected in the Cu_2MnSiS_4 sample. Therefore, additional materials were added to the model. The final refinement indicated that Cu_2MnSiS_4 was the major phase (mass % = 96.7%), though small amounts of unwanted Mn_5Si_3 (mass % = 1.92%) and Cu_2SiS_3 (mass % = 1.38%) existed in the sample (Figure 2a). A peak near 5.9 Å was excluded because its intensity mainly stems from the magnetic contribution from the Mn_5Si_3 impurity phase, which orders antiferromagnetically with T_N ~ 100 K.[27] The Cu_2FeSiS_4 sample was assessed as being phase pure, as the NPD data at 100 K could be completely accounted for with the single Cu_2FeSiS_4 phase (Figure 2b).

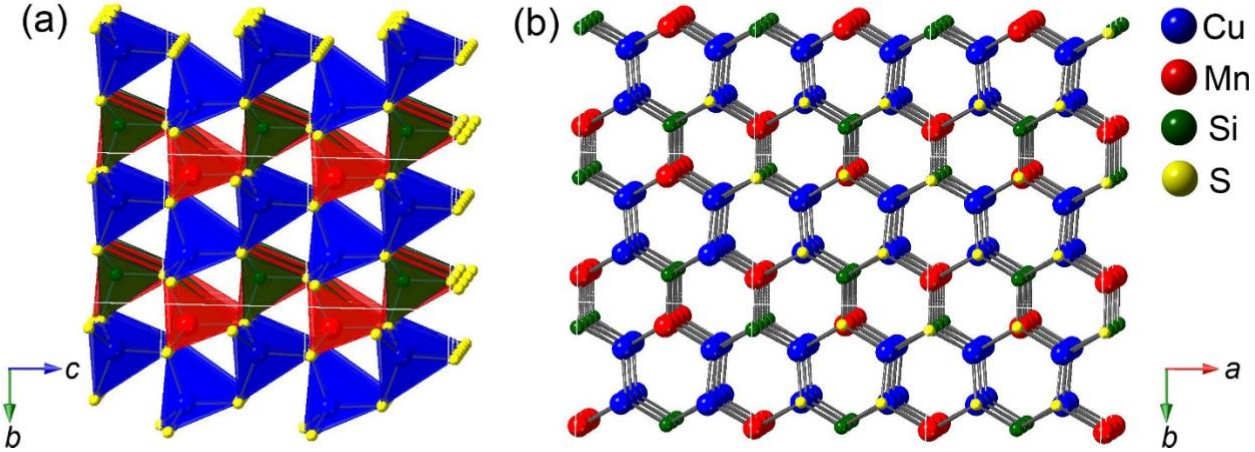

Figure 1: Perspective view of the crystal structure of Cu_2MnSiS_4 along the crystallographic *a* axis (a) and *c* axis (b).

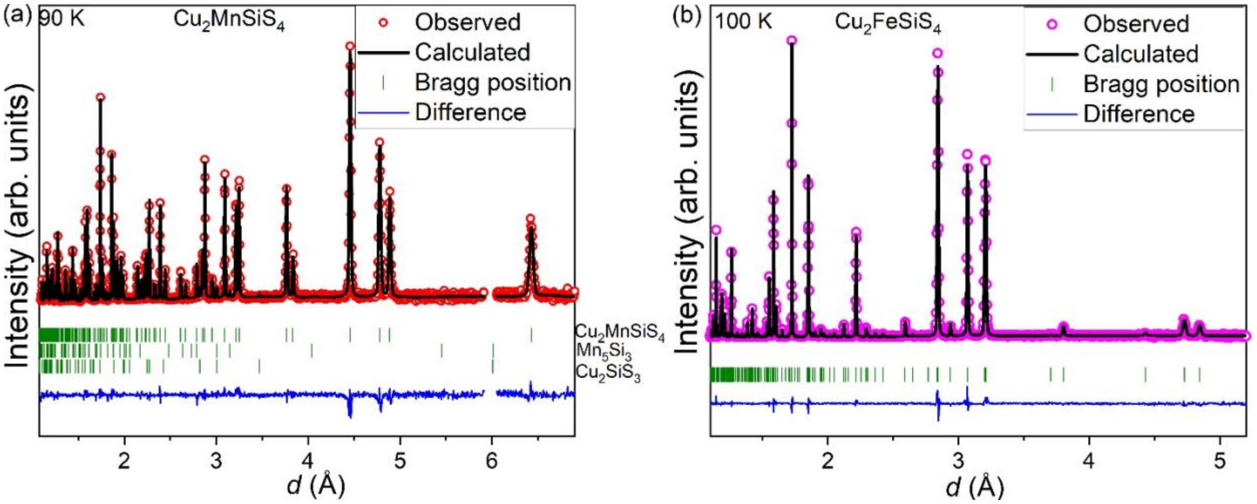

Figure 2. Rietveld refinement of Cu_2MnSiS_4 (a) and Cu_2FeSiS_4 (b) in the space group $Pmn2_1$ using NPD data. The observed data (red), calculated pattern (black), and the difference between those two patterns (blue) are provided. The expected Bragg peak positions (green) of nuclear reflections are also depicted.

Selected refinement parameters and fractional atomic coordinates are given in Table 1. The refined unit cell parameters of Cu_2MnSiS_4 at 90 K are slightly smaller than those refined using room-temperature single crystal X-ray diffraction data [a = 7.5431(1) Å, b = 6.4401(1) Å, c = 6.1877(1) Å, and V = 300.229(8) Å^3], and previously reported values for Cu_2MnSiS_4 at 293 K [a = 7.543(2) Å, b = 6.446(1) Å, c = 6.193(1) Å, and V = 301.1(1) Å^3].[15] The refined unit cell parameters of Cu_2FeSiS_4 at 100 K are also close to those refined using room temperature single crystal X-ray diffraction data [a = 7.4162(1) Å, b = 6.4121(1) Å, c = 6.1397(1) Å, and V = 291.964(8) Å^3], and published values for Cu_2FeSiS_4 at 293 K (a =

7.404 Å, b = 6.411 Å, c = 6.14 Å, and V = 291.45 Å^3).[12] The unit cell volume of Cu_2MnSiS_4 is slightly larger than that of Cu_2FeSiS_4, which is because the ionic radius of Mn^{2+} (0.66 Å) ion is larger than that of Fe^{2+} ion (0.63 Å).[28]

Table 1. Selected Structure Parameters and Refinement Details for Cu_2TSiS_4 (T = Mn and Fe) using NPD Data

nominal composition		Cu_2MnSiS_4		Cu_2FeSiS_4	
refined formula		Cu_2MnSiS_4		Cu_2FeSiS_4	
temperature		90 K	2 K	100 K	2 K
mol. wt.		338.38		339.28	
density, g/cm^3 (calculated)		3.759	3.760	3.872	3.875
space group, #		$Pmn2_1$, # 21		$Pmn2_1$, # 21	
Z		2		2	
lattice parameters		a = 7.5264(1) Å, b = 6.4250(1) Å, c = 6.1823(1) Å, V = 298.957(1) Å^3	a = 7.5262(2) Å, b = 6.4237(1) Å, c = 6.1817(1) Å, V = 298.86(1) Å^3	a = 7.4119(1) Å, b = 6.3985(1) Å, c = 6.1352(1) Å, V = 290.964(8) Å^3	a = 7.4115(1) Å, b = 6.39656(8) Å, c = 6.13509(8) Å, V = 290.854(7) Å^3
Rietveld criteria of fit of major nuclear phase		R_p = 3.98%, R_{wp} = 3.17%, R_{exp} = 1.82%, χ^2 = 3.04	R_p = 5.17%, R_{wp} = 4.44%, R_{exp} = 1.32%, χ^2 = 11.3	R_p = 3.27%, R_{wp} = 2.65%, R_{exp} = 1.48%, χ^2 = 3.21	R_p = 3.23%, R_{wp} = 3.44%, R_{exp} = 0.9%, χ^2 = 14.6
Site	Wyckoff symbol	x, y, z	x, y, z	x, y, z	x, y, z
Cu	4b	0.7528(2), 0.6781(2), 0.178(1)	0.7531(2), 0.6781(3), 0.178(1)	0.2476(2), 0.3248(3), 0.013(2)	0.2476(2),0.3257(3), 0.012(2)
Mn (Fe)	2a	0, 0.8441(7), 0.670(3)	0, 0.842(1), 0.666(2)	0, 0.1541(3), 0.500(3)	0, 0.1548(3), 0.499(2)
Si	2a	0, 0.1748(7), 0.178(3)	0, 0.1768(9), 0.187(2)	0, 0.8298(8), 0	0, 0.8300(7), 0
S1	2a	0, 0.858(1), 0.062(1)	0, 0.860(1), 0.065(2)	0, 0.814(1), 0.350(2)	0, 0.816(1), 0.349(2)
S2	2a	0, 0.183(1), 0.515(1)	0, 0.187(1), 0.518(1)	0, 0.141(1), 0.885(2)	0, 0.141(1), 0.883(2)
S3	4b	0.7304(6), 0.6668(9), 0.550(1)	0.7313(8), 0.668(1), 0.552(1)	0.2643(8), 0.329(1), 0.388(1)	0.2651(8), 0.329(1), 0.388(1)

Table 2. Selected Bond Distances in Cu_2TSiS_4 (T = Mn and Fe) Refined at 90 and 100 K, respectively

Cu_2MnSiS_4 Cu/Mn/Si-S distances (Å)		Cu_2FeSiS_4 Cu/Fe/Si-S distances (Å)	
Cu-S1	2.304(6)	Cu-S1	2.300(8)
Cu-S2	2.333(4)	Cu-S2	2.318(9)
Cu-S3	2.31(1)	Cu-S3	2.31(1)
Cu-S3	2.356(7)	Cu-S3	2.342(8)
Mn-S1	2.43(2)	Fe-S1	2.361(1)

Mn-S2	2.377(9)	Fe-S2	2.364(2)
Mn-S3 (×2)	2.440(8)	Fe-S3(×2)	2.359(7)
Si-S1	2.16(1)	Si-S1	2.15(1)
Si-S2	2.08(2)	Si-S2	2.11(1)
Si-S3 (×2)	2.158(9)	Si-S3 (×2)	2.135(7)

As shown in Figure 1, the crystal structure of Cu_2TSiS_4 (T = Mn and Fe) consists of CuS_4, TS_4 (T = Mn and Fe), and SiS_4 tetrahedra. In each tetrahedron, Cu/Mn/Fe/Si coordinates with one S1 atom, one S2 atom, and two S3 atoms, with slightly different bond distances (d) within the respective tetrahedra (Table 2). The refined d(Cu-S) and d(Si-S) in the two Cu_2TSiS_4 (T = Mn and Fe) compounds are very close in most instances or identical in some instances, considering the estimated standard deviations. As expected, the d(Mn-S) is longer than d(Fe-S). The refined d(Cu-S) = 2.30-2.36 Å and d(Mn-S) = 2.38-2.44 Å are very close to those found in the isostructural Cu_2MnGeS_4 compound [d(Cu-S) = 2.31-2.35 Å and d(Mn-S) = 2.43-2.46 Å].[15] The obtained d(Si-S) = 2.08-2.16 Å is in good agreement with the d(Si-S) = 2.14 Å observed in Cu_2CoSiS_4 with the space group $I\bar{4}2m$.[12] Because there are four different bond distances in CuS_4 tetrahedron and three unequal bond distances in MnS_4, FeS_4, and SiS_4 tetrahedra, all of the tetrahedra are distorted, and the chains of corner-sharing tetrahedra are unsymmetrical as shown in Figure 1a. When looking at the projection along the crystallographic c axis, all atoms are connected in distorted hexagonal, i.e., honeycomb, patterns containing three sulfide anions and three metal cations (Figure 1b). Such an arrangement of connected, distorted tetrahedra explains the polar crystal structure, and the more distorted CuS_4 tetrahedron contributes most to the polarization.

Electron Diffraction. To confirm the refined crystal structure of Cu_2TSiS_4 (T = Mn and Fe) obtained from NPD, TEM experiments were performed. An SAED pattern of the Cu_2MnSiS_4 sample was obtained along the [100] direction. It is consistent with the simulated pattern of Cu_2MnSiS_4 with the space group $Pmn2_1$. The (010) diffraction spot has similar intensity as the (020) spot, and the extinct (001) spot has intensity due to the double diffraction, which is a typical phenomenon of the dynamical scattering of a thick crystal. The corresponding atomic resolution HAADF-STEM image shows rows of alternate bright and weak spots and a neighboring row of weaker spots. Because the atomic column image intensity in the HAADF-STEM image is almost proportional to the atomic number (Z^2) of an atom and the number of that atom along the column, the heavier the atom, the brighter the spots. Therefore, the intensity of Cu (Z = 29) is the brightest, the mixed columns of Mn (Z = 25) and Si (Z =14) have an average atomic number of 19.5 and are less bright, and S columns (Z = 16) are the weakest. In Figure 3b, rows with alternate bright and weak spots are the rows of Cu atoms and Si/Mn atoms in the crystal structure of Cu_2MnSiS_4 with the space group $Pmn2_1$ (Figure 3c). The adjacent rows with weaker spots in Figure 3b correspond to the S atoms in the crystal structure (Figure 3c).

The electron diffraction pattern recorded from a single piece of Cu_2FeSiS_4 can be indexed to the [001] direction with the space group $Pmn2_1$ (Figure 4a). The extinct (100) spot that has intensity is due to the double diffraction. The corresponding atomic resolution HAADF-STEM image shows a pattern consisting of hexagonal spots, which correspond well with the crystal structure viewed along the [001] direction (Figure 4b, c). Along this projected direction, all atomic columns are mixed with S. So the average atomic number for Cu/S is 22.5, 21 for Fe/S mixed column, and 15 for Si/S columns. The atomic number difference between Cu/S and Fe/S is 1.5, which is too small to have an intensity difference. So these columns should have similar bright intensity. But the Fe/S should be easily identifiable with weak intensity. Therefore, the rows of bright spots with the same intensity represent the atomic Cu/S atomic columns, and the neighboring rows with alternating weak and strong spots correspond to the rows of Si/S and Fe/S atoms. A HAADF-STEM image was also collected along the [100] direction; it shows alternating bright and dim spots, indicating the ordering of Fe/Si and Cu, similar to that observed for the Cu_2MnSiS_4 crystal.

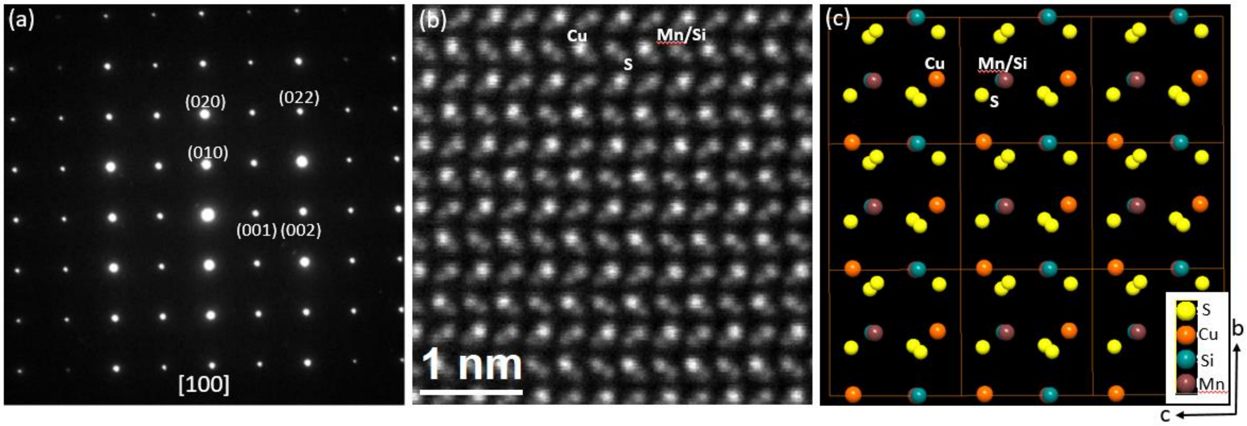

Figure 3. (a) Electron diffraction pattern along the [100] direction, (b) atomic resolution HAADF-STEM image, and (c) perspective view of the crystal structure of Cu_2MnSiS_4 with the space group $Pmn2_1$.

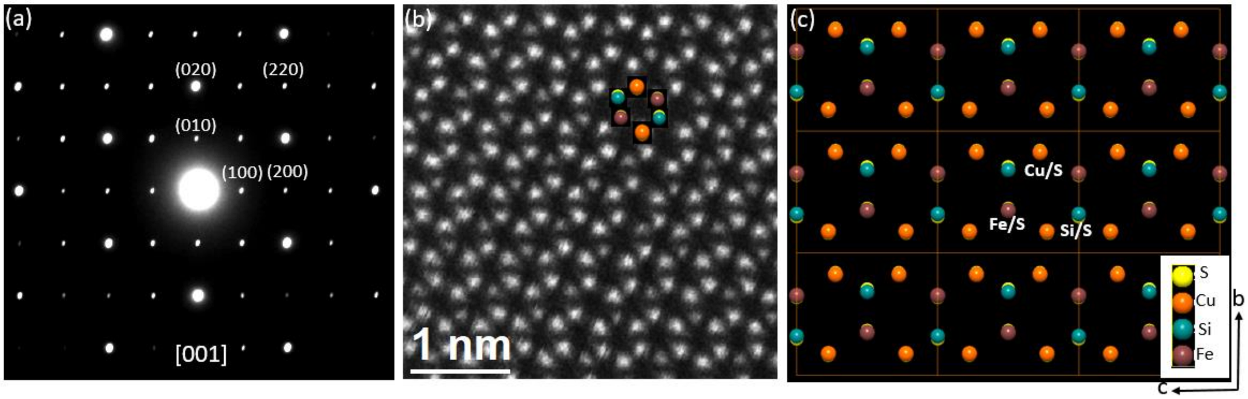

Figure 4. (a) Electron diffraction pattern along the [001] direction, (b) atomic resolution HAADF-STEM image, and (c) perspective view of the crystal structure of Cu_2FeSiS_4 with the space group $Pmn2_1$.

However, for some crystals, the electron diffraction indicates the absence of (010) reflection, and the HAADF-STEM image shows rows of spots with the same intensity, indicating the disorder of Cu with Fe/Si in the crystal structure (Figure S2). The possible disorder structure might be similar to that of $Cu_2CoGeSe_4$ with the $F222$ space group, in which Cu, Co, and Ge are disordered and occupy the $4a$ (0, 0, 0) site in the crystal structure.[12] Another disordered crystal structure in the CTMS-related system is $Cu_2NiSnSe_4$ ($F\bar{4}3m$), with Cu, Ni, and Sn atoms also occupying the $4a$ (0, 0, 0), same as the above site.[12] The XRPD of this possible disordered structure is different from the polar crystal structure of $Pmn2_1$, and the corresponding peaks are not present in our patterns, indicating that the amount of such a disordered sample is too small to be detected in our X-ray or neutron powder patterns. The magnetic and optical properties should not be measurably affected by these small inclusions.

Chemical Analysis. Semi-quantitative SEM-EDX measurements were performed on Cu_2TSiS_4 (T = Mn and Fe) crystals. The EDX maps of the selected area (~ 100 μm × 100 μm) of the surface of the crystal indicate that the Cu, Mn, Si, and S elements are homogeneously distributed (Figure 5). The calculated molar ratio of Cu:Mn:Si:S is 1.93:1:1.08:4.29, which is close to the expected 2:1:1:4 ratio. Similar homogenous distribution of Cu, Fe, Si, and S elements is also observed in the Cu_2FeSiS_4 crystal with the obtained molar ratio of Cu:Mn:Fe:S = 1.95:1:1.02:4.08 (Figure S3).

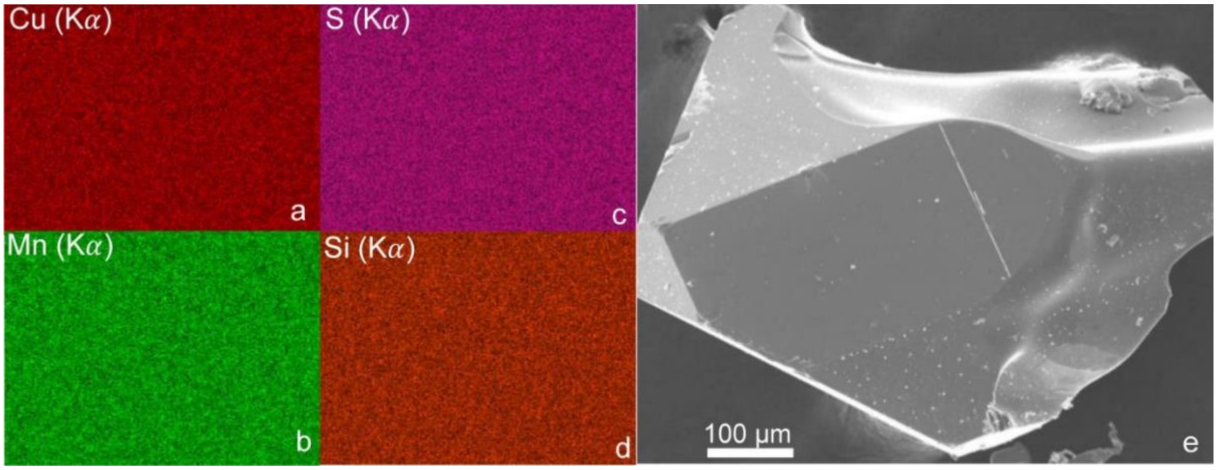

Figure 5. (a-d) EDX elemental maps and (e) SEM micrograph of a Cu_2MnSiS_4 single crystal.

Magnetic Properties.

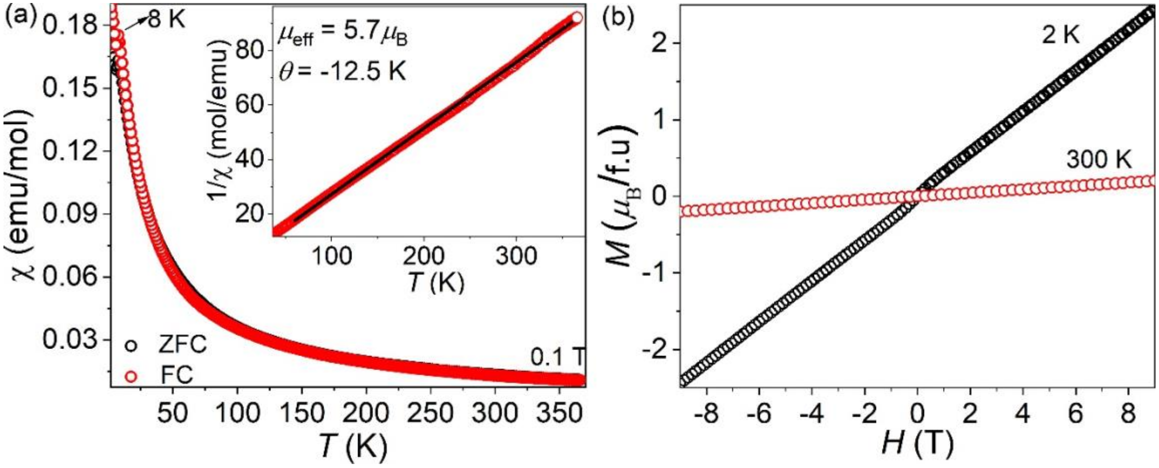

Figure 6. (a) Temperature-dependent ZFC-FC and (b) field-dependent magnetization of polycrystalline Cu_2MnSiS_4.

ZFC-FC magnetic measurements on polycrystalline Cu_2MnSiS_4 and Cu_2FeSiS_4 samples show antiferromagnetic (AFM) ordering at 8 (Figure 6) and 14 K (Figure 7), respectively, which are consistent with the reported values (8 and 15 K) as shown in Table 3.[16] The Curie-Weiss ($\chi = C/(T - \Theta_w)$ fitting of the inverse high-temperature magnetic susceptibility gives a negative Weiss constant Θ_w = -12.5 and -19.5 K for Cu_2MnSiS_4 and Cu_2FeSiS_4, respectively, indicating AFM coupling between Mn/Fe moments. The $\mu_{eff}(Mn^{2+})$ obtained from the Curie-Weiss fitting of Cu_2MnSiS_4 data is 5.7 μ_B, which is also close to the theoretical value of $\mu_{eff}(Mn^{2+})$ = 5.92 μ_B, and the reported values (μ_{eff} = 5.9 μ_B, Θ_w = -17 K) for Cu_2MnSiS_4.[29] The μ_{eff}(Fe) obtained from the Curie-Weiss fitting of Cu_2FeSiS_4 data is 5.13 μ_B, which is close to the theoretical value of $\mu_{eff}(Fe^{2+}) = 4.9\ \mu_B$. The linear behavior of field-dependent magnetization at 2 K also confirms the AFM ordering. The AFM ordering with low T_N has also been observed in other $Cu_2T^{II}M^{IV}S_4$ (T = Mn, Fe, Co, and Ni; M = Si, Ge, and Sn), as shown in Table 3.

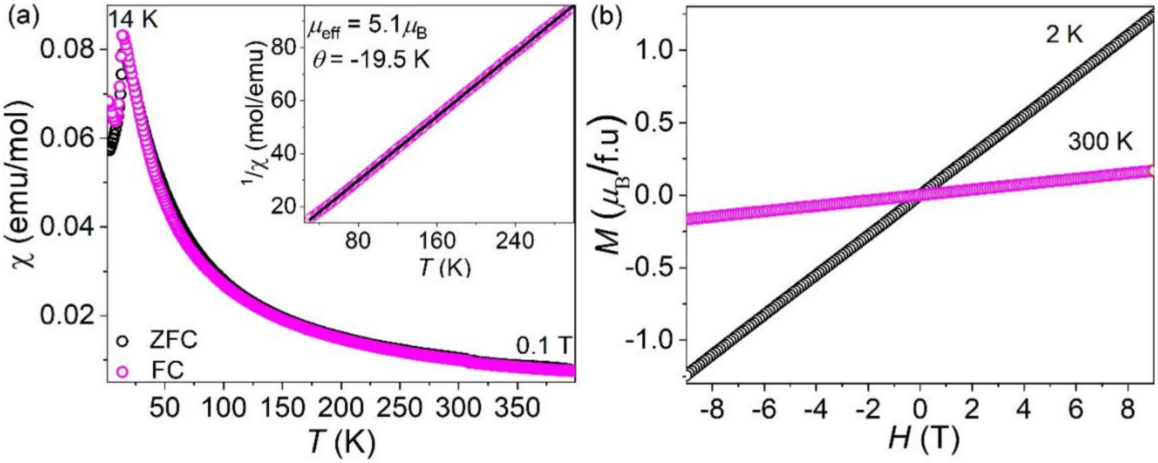

Figure 7. (a) Temperature-dependent ZFC-FC and (b) field-dependent magnetization of polycrystalline Cu_2FeSiS_4.

Table 3. Summary of Magnetic Properties of Cu_2TMS_4 (T = Mn, Fe, Co, and Ni; M = Si, Ge, and Sn)

compound	space group	T_N, K	*k* vector	magnetic space group	references
Cu_2MnSiS_4	$Pmn2_1$	8, 8*	(½,0,½)*	P_ac*	16, 29
Cu_2FeSiS_4	$Pmn2_1$	15, 14*	(½,½,½)*	C_ac*	12, 16
Cu_2CoSiS_4	$I\bar{4}2m$	-	-	-	30
Cu_2NiSiS_4	-	-	-	-	
Cu_2MnGeS_4	$Pmn2_1$	8.3, 9	(½,0,½)	P_ac	13, 15, 16, 31, 32
Cu_2FeGeS_4	$I\bar{4}2m$	12, 17	(½,0,½)	-	12, 16, 29, 33
Cu_2CoGeS_4	$I\bar{4}2m$	25	-	-	29, 30
Cu_2NiGeS_4	$I\bar{4}2m$, $I\bar{4}$	36	-	-	29, 34, 35
Cu_2MnSnS_4	$I\bar{4}2m$	8.8, 10	(½,0,½)	P_a2_1	13, 15, 16, 36, 37
Cu_2FeSnS_4 (β)	$I\bar{4}2m$	6.1, 7, 8	-	-	9, 38, 39, 40
Cu_2FeSnS_4 (α)	$P\bar{4}$	38	-	-	11, 41
Cu_2CoSnS_4	$I\bar{4}2m$	-	-	-	30
Cu_2NiSnS_4	$F43m$	-	-	-	12

*this work

Neutron Diffraction. Among the reported compounds of the CTMS family, only Cu_2MnGeS_4, Cu_2MnSnS_4, and Cu_2FeGeS_4 have had their magnetic structures investigated (Table 3).[13,33] To determine the magnetic structures of Cu_2MnSiS_4 and Cu_2FeSiS_4, NPD measurements were performed between 90-2 K and 100-2 K, respectively. Selected NPD patterns are shown in Figure 8. For the Cu_2MnSiS_4 sample, the pattern remains the same as the temperature decreases from 90 to 7.5 K, but new magnetic reflections show up below approximately 7.5 K, and their intensities increase as the temperature decreases. The observation of magnetic reflections at 7 K confirms the AFM transition determined by the magnetic measurements (Figure 6a). By comparison of the NPD patterns of 90 and 2 K (Figure S4), the obvious six magnetic reflections appearing at a lower temperature can be identified at 9.3 Å, 5.3 Å, 4.65 Å, 3.97 Å, 3.38 Å, and 3.04 Å. For the Cu_2FeSiS_4 sample, new magnetic reflections appear below 14 K, which also supports the AFM ordering observed in the magnetic data (Figure 7a). The intensity of magnetic reflections increases as the temperature decreases to 2 K (Figure 8b). There are eight obvious peaks attributed to the magnetic structure being located at 7.6 Å, 4.31 Å, 3.89 Å, 3.77 Å, 3.12 Å, 2.89 Å, 2.54 Å, and 2.47 Å (Figure 8b, S4).

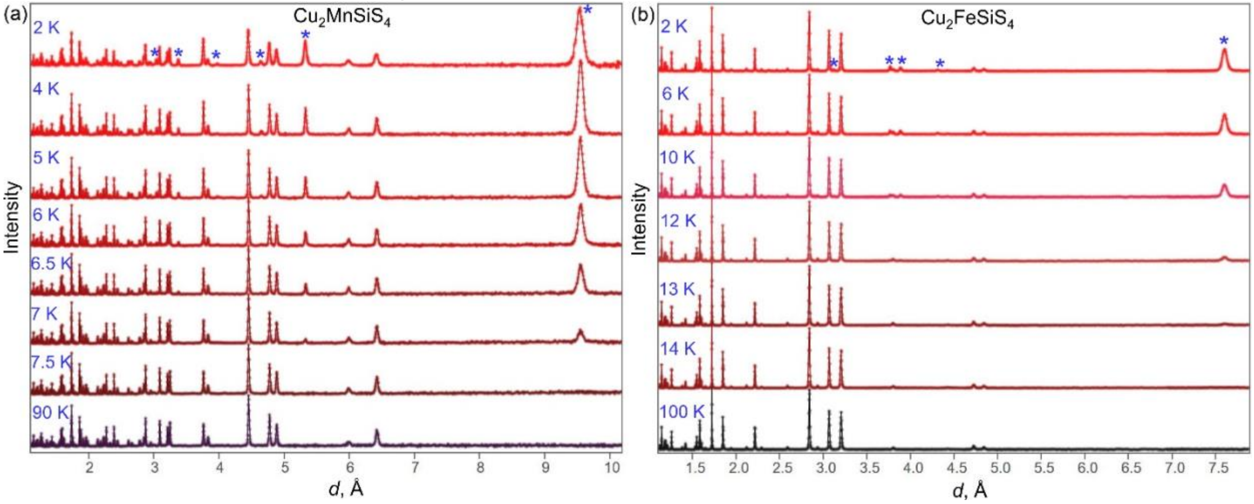

Figure 8. (a) Selected NPD patterns of Cu_2MnSiS_4 between 90 and 2 K and (b) Cu_2FeSiS_4 between 100 and 2 K (b). Magnetic peaks are marked with a star (*) symbol. For clarity purposes, only a few strongest peaks are marked.

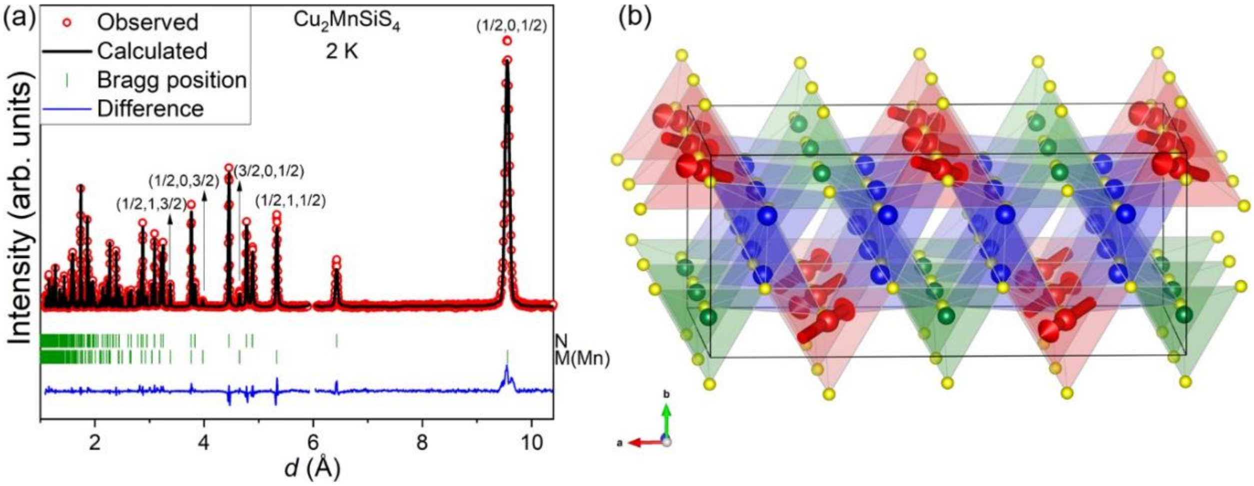

Figure 9. (a) Rietveld refinement of Cu_2MnSiS_4 (space group *Pmn*2_1) using NPD data (2 K) with observed data (red), calculated pattern (black), and the difference between the observed and calculated patterns (blue), and Bragg peak positions of major nuclear and magnetic reflections (green). (b) Magnetic structure of Cu_2MnSiS_4 (color code: Cu = blue, Mn = red, Si = green, and S = yellow).

In the NPD data of Cu_2MnSiS_4 collected at 2 K, the observed magnetic peaks can be indexed using the magnetic propagation vector k = (½,0,½), with the most intense peak (½,0,½), located at 9.3 Å. The nuclear peaks observed at 2 K can be fit well with the same nuclear structure model used for the 90 K data set (Figure 9a). The refined unit cell parameters and atomic positions show a very small difference between the two temperatures (Table 1). The only magnetic ions in the unit cell are Mn^{2+} ions occupying only one Wyckoff position, 2*a*. The best-fitting magnetic structure model involves an alignment of Mn magnetic moments along the MnS_4 tetrahedral edge, with the Mn pair inside the chemical unit cell having the m_a and m_c components parallel but the m_b components antiparallel to each other. The moments are alternating their directions along the *a* and *c* directions resulting in an overall antiferromagnetic structure. The determined magnetic structure is shown in Figure 9b, with the magnetic unit cell doubled in *a* and *c* directions as compared to the nuclear structure. This magnetic structure adopts the magnetic space group P_ac (#7.27).[19] The refined magnetic components of Mn at 2 K are m_a = 2.25(5) μ_B, m_b = 1.0(1) μ_B, and m_c = -3.18(5) μ_B, which yields a total magnetic moment m_{Mn} = 4.1(1) μ_B. The canting angle away from the *ac* plane is about 14°. Other refined parameters of the magnetic structure are given in Table S4.

This magnetic propagation vector of Cu_2MnSiS_4 is the same as that of isostructural Cu_2MnGeS_4, and stannite Cu_2MnSnS_4 ($I\bar{4}2m$),[13,36] and the refined magnetic moment (4.1 μ_B) for Cu_2MnSiS_4 is just slightly smaller than those obtained for the other compounds: ~4.3 μ_B (Cu_2MnGeS_4) and ~4.28 μ_B (Cu_2MnSnS_4).[13,36] The isostructural Cu_2MnGeS_4 has been reported to order with the same magnetic space group symmetry P_ac but the moments are rotated from the *c*-direction towards the *b*-axis ($m_a \approx$ 2.6 μ_B, m_b = 3.3 μ_B, and m_c = 0.9 μ_B).[13] Cu_2MnSnS_4 exhibits a collinear AFM magnetic structure (magnetic space group P_a2_1) with *k* = (½,0,½), in which the magnetic moments are constrained by symmetry to lie in the *ac* plane (m_b = 0 μ_B). Nevertheless, the moments are still mainly oriented towards the edge of the MnS_4 tetrahedra with a small deviation of 11+/-5° away from the crystallographic *c* axis.[36]

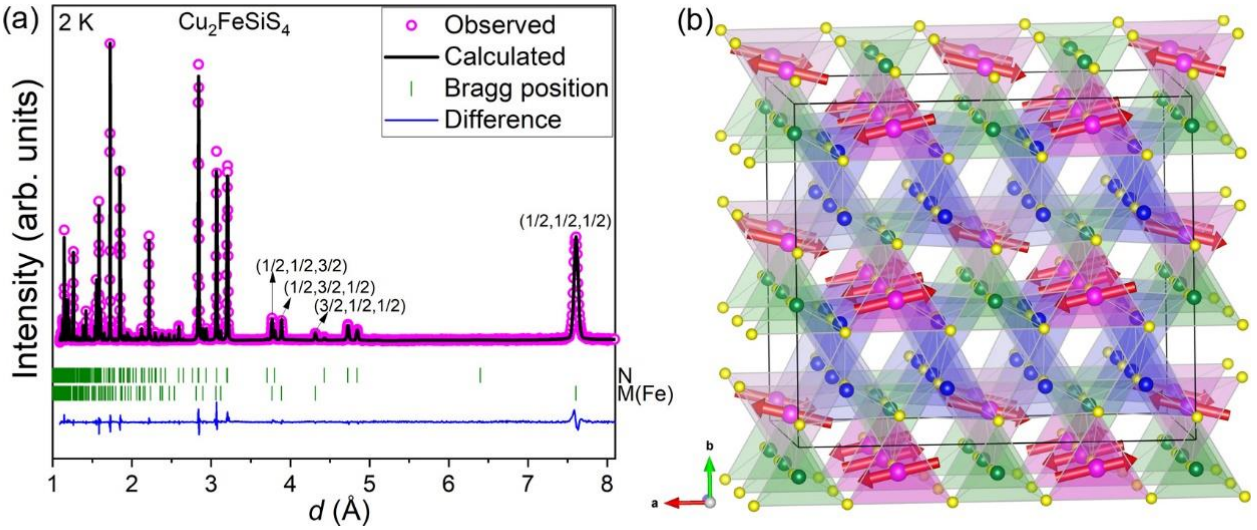

Figure 10. (a) Rietveld refinement of Cu_2FeSiS_4 (space group $Pmn2_1$) using NPD (2 K) data, with observed data (red), calculated pattern (black), and the difference between the observed and calculated patterns (blue), and Bragg peak positions of nuclear and magnetic reflections (green). (b) Magnetic structure of Cu_2FeSiS_4 (color code: Cu = blue, Fe = magenta, Si = green, and S = yellow).

The magnetic peaks that appear in the low temperature (T < 14 K) NPD data of Cu_2FeSiS_4 can be indexed by the wave-vector *k* = (½,½,½). The nuclear contribution to the NPD data collected at 2 K can be fit well using the same structural model as that used for the refinement using the data obtained at 100 K (Figure 10a). The refined unit cell parameter and atomic positions remained almost the same. The determined magnetic structure model that accounts well for all magnetic intensities is displayed in Figure 10b. Similar to Cu_2MnSiS_4, the two equivalent sites of the nuclear cell [(Fe^{2+} located at (0, 0.155, 0.509) and (0.5, 0.845, 0.009)] have parallel m_a and m_c components but antiparallel m_b. The magnetic moments alternate their directions along all three crystallographic directions leading to a magnetic unit cell eight times larger than the nuclear lattice. The corresponding magnetic space group is C_ac (#9.41). The refined magnetic components of Fe at 2 K are: m_a = 2.85(3) μ_B, m_b = 0.7(1) μ_B, and m_c = 0.5(1) μ_B, which yields a total magnetic moment of 2.9(1) μ_B. The spins axis is oriented at about 14°

from the *ac* plane, which is very similar to the canting determined for the Mn congener. Other refined parameters of the magnetic structure are given in Table S5.

The determined magnetic structures for both investigated compounds can be viewed as consisting of chains of collinear spins that are arranged antiferromagnetically along the *c* direction. The magnetic moments of adjacent chains are canted with respect to each other around the *b* axis. While in the Mn compound, the direction of the spins only alternates inside the chain (*c* axis) and along the *a* axis, in the Cu_2FeSiS_4 compound, the Fe spins are alternating their orientation in all crystallographic directions. A propagation vector k = (½,0,½) has been observed for all studied Mn systems [Cu_2MnSiS_4, Cu_2MnGeS_4, Cu_2MnSnS_4 ($I\bar{4}2m$)], and also for Cu_2FeGeS_4 ($I\bar{4}2m$).[13,33,36] In the latter, four distinct magnetic structure models compatible with the propagation vector k = (½,0,½) have been discussed, but the final model was not determined.[33] The magnetic structure of the other related Fe-containing sulfide, Cu_2FeSnS_4, has not been reported. Considering selenides and tellurides as well, Cu_2FeGeS_4 is the first example with a k = (½,½,½) magnetic order in the quaternary Cu_2FeMX_4 (M = Si, Ge, and Sn; X = S, Se, and Te) chalcogenides family. The propagation vector k = (½,½,½) and a similar magnetic moment of Fe (2.82 μ_B) have also been observed in the related Li_2FeGeS_4, a polar (space group *Pn*) antiferromagnet (T_N ~ 6 K) with collinear magnetic Fe spins along the *b* axis, which is different from the incommensurate [k = (0,0,0.546)] collinear magnetic structure in the polar (space group *Pn*) antiferromagnet (T_N ~ 4 K) Li_2FeGeS_4.[42]

Attenuated Total Reflectance Fourier Transform Infrared Spectroscopy. ATR FT-IR spectroscopy was used to assess the windows of optical clarity for Cu_2TSiS_4 (T = Mn and Fe). Accurate and extreme transparency necessary for NLO devices should be determined using high-quality, single crystal specimens, but ATR FT-IR of microcrystalline samples provides a general idea of the transparency. As expected for sulfides, the IR transparency is very high, with both compounds exhibiting values above 80% transparency throughout the entire measured range of 2.5 to 25 μm (Figure S5).

Second-order NLO Property Measurements. Using an incident wavelength of λ = 1800 nm, the SHG dependence on the particle size was investigated for the title compounds and compared to those of the NLO reference materials. The AGS reference exhibits a clear phase matching (PM) trend, as indicated by increasing SHG counts with increasing particle size. This result is consistent with the known PM onset, which is indeed λ = 1800 nm for AGS. On the other hand, the SHG response of the title compounds does not increase with increasing particle size, signifying that they are non-phase matching (NPM) at this wavelength. Normally, broadband NLO studies would be performed to search for a possible PM onset, as most related compounds that have been studied are PM at some longer wavelengths; however, this was not possible for the title compounds. The Cu_2TSiS_4 (T = Mn and Fe) samples did not exhibit enough SHG counts in the mid-IR, λ > 2400 nm, to be detected by an InGaAs detector, and they did not have a measurable response for λ = 1064 nm either. Therefore, the SHG coefficients of the title compounds were assessed by comparing them with the SHG counts from AGSe, which is also NPM at λ = 1800 nm.

It should be noted that because the title compounds did not exhibit a measurable SHG response at λ = 1064 nm, the laser-induced damage thresholds (LIDTs), which are almost always reported for λ

= 1064 nm, could not be assessed. However, given the relatively narrow optical bandgaps of the title compounds, outstanding LIDTs are not anticipated.

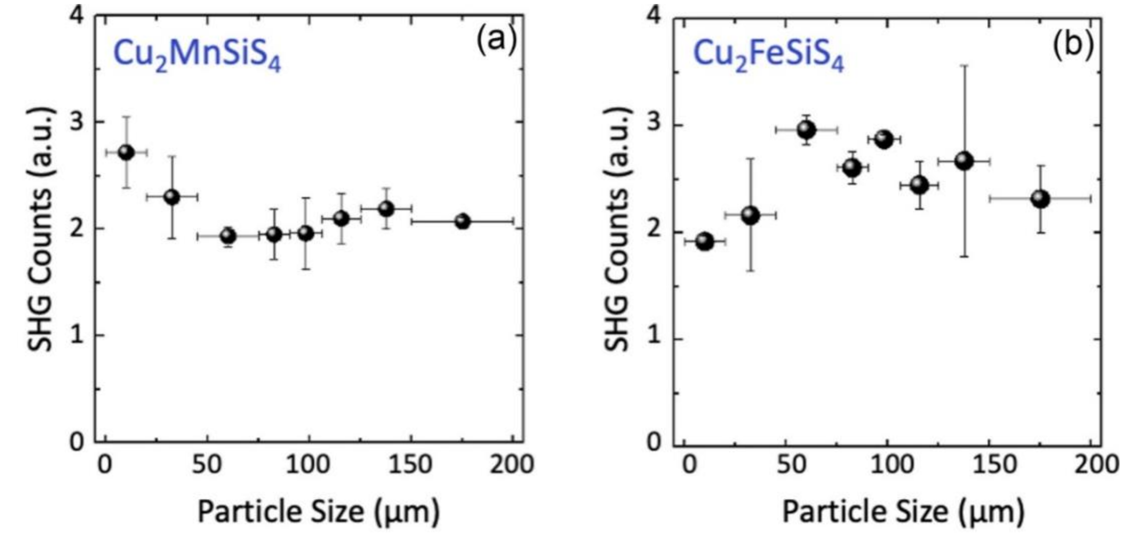

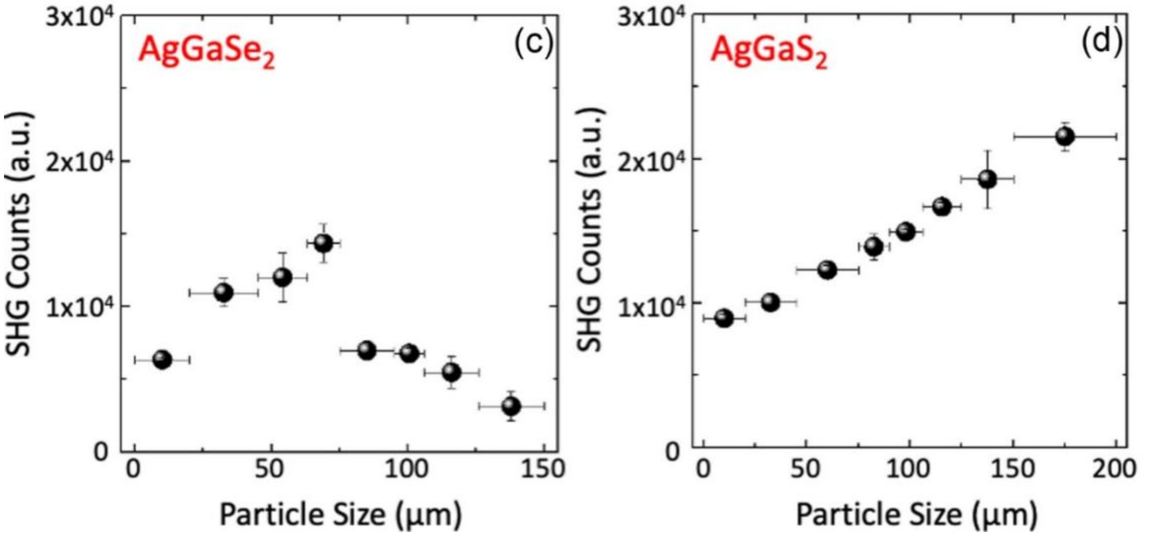

Figure 11. Particle size dependence of the SHG response for Cu$_2$MnSiS$_4$ and Cu$_2$FeSiS$_4$ (a, b) compared to that of the AGSe and AGS reference materials (c, d). At this incident wavelength, λ = 1800 nm (i.e. λ_{SHG} = 900 nm), only the AGS is phase matchable.

The second-order NLO susceptibility of each sample, $\chi_S^{(2)}$, was calculated by comparing with that of AGSe using the Kurtz powder method for the NPM case;[43] where I_S^{SHG} and I_R^{SHG} are the experimentally measured SHG counts from the test sample and the reference, respectively.

$$\chi_S^{(2)} = \chi_R^{(2)} \frac{l_R}{l_S} \left(\frac{I_S^{SHG}}{I_R^{SHG}}\right)^{1/2}, \qquad (1)$$

In equation (1), l_S and l_R are the experimentally measured coherence lengths that correspond to the maximum SHG counts in Figure 11. Using $\chi_R^{(2)}$ ~ 66 pm/V for AGSe,[44] our calculation yields $\chi_S^{(2)}$(Cu$_2$MnSiS$_4$) ~ 6.27±0.07 pm/V and $\chi_S^{(2)}$(Cu$_2$FeSiS$_4$) ~ 1.09±0.03 pm/V, respectively. Although both compounds exhibit rather similar SHG counts, the difference in $\chi_S^{(2)}$ arises from the difference in the coherence lengths. While both title compounds definitely yield a finite SHG response, the SHG intensities are quite weak compared with AGSe and AGS ($\chi_R^{(2)}$~ 36 pm/V)(b),[45] which are benchmark IR-NLO materials, and the resulting $\chi_S^{(2)}$ values are expectedly modest.

To put things into perspective, one can consider these results for the title compounds in the context of other quaternary chalcogenides with the same or similar crystal structures. Though the nonpolar $Cu_2ZnGeSe_4$ with the kesterite structure has a similar bandgap (1.38 eV) to Cu_2MnSiS_4, it has a much better SHG performance with $\chi_S^{(2)}$ ~ 43 pm/V. On the other hand, the polar $Cu_4ZnGe_2Se_7$, which has a more complex superstructure of zinc blende and narrower optical bandgap (0.91 eV), only exhibited a very weak SHG response, such that the $\chi_S^{(2)}$ value was not determined. The polar Li_2MnGeS_4 with a different superstructure of the W structure demonstrates a similar SHG efficiency as Cu_2MnSiS_4, $\chi_S^{(2)}$~ 6.6 pm/V, though the optical bandgap of the former is much wider (3.07 eV). Some other compounds with the same WSt structure as the title compounds, such as Cu_2MnGeS_4 and Li_2CdGeS_4, have much stronger SHG responses with $\chi_S^{(2)}$~ 16.9 pm/V and $\chi_S^{(2)}$~ 22.5 pm/V, but also considerably larger optical bandgaps of 2.21 and 3.15 eV, respectively. In a nutshell, the performance of the title compounds lies in the same realm as related materials, which vary widely in their SHG responses and optical bandgap energies.

Electronic Structure Calculations. DFT calculations were carried out to investigate the electronic structure of Cu_2MSiS_4 (M = Mn and Fe). From the NPD experiments, these systems show canted AFM ordering. In the magnetic DFT calculations, however, collinear AFM structures were used instead for both systems for simplicity. This simplification might change the details of the electronic structure but does not alter the general conclusion of this study.

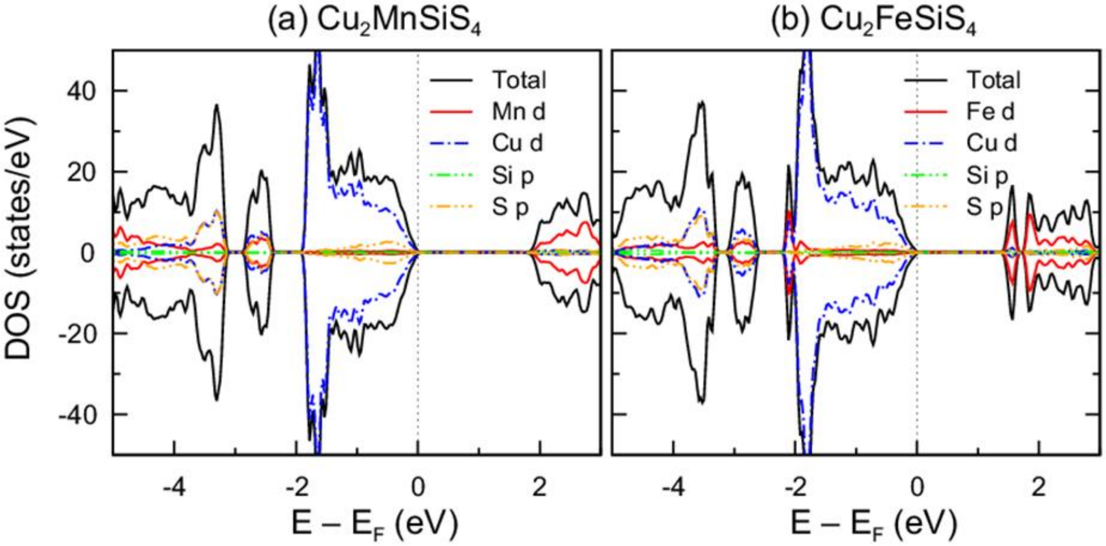

Figure 12. Total and partial densities of states (DOS) of Cu_2MnSiS_4 (a) and Cu_2FeSiS_4 (b) with collinear AFM structures. The positive and negative values in DOS correspond to spin-up and-down configurations, respectively.

DFT calculations were performed with on-site Coulomb repulsion parameters U_{eff} = 4 eV and 5 eV chosen for Cu_2MnSiS_4 and Cu_2FeSiS_4, respectively. Those values are comparable to those used in previous DFT studies on similar compounds.[46,47] The densities of states (DOS) for both systems with collinear AFM structures are presented in Figure 12. The DFT calculations show that both systems are semiconductors with bandgaps > 1 eV. The bandgap is formed between the top of the valence band with mostly Cu-*d* character and the bottom of the conduction band with mostly Mn (Fe)-*d* character in the case of Cu_2MnSiS_4 (Cu_2FeSiS_4). The character of dominating Cu-*d* orbitals near valence band maximum (VBM) is also observed in Cu_2MGeS_4 (T = Mn and Ni), and Cu_2TSnS_4 (M = Mn, Fe, and Ni),[48,49,46,50] which is different from the character of hybridization of Cu-*d* and S-*p* found in Cu_2CoMS_4 (M = Ge, Sn).[51,52] The feature of T-*d* orbitals near the conduction band minimum (CBM) of Cu_2TSiS_4 (T = Mn and Fe) is similar to that of Cu_2NiMS_4 (M = Ge and Sn),[35,49,50] and Cu_2CoGeS_4,[51] which is different from the hybridization of Mn-*d*, Ge-*s*, and S-*p* in Cu_2MnGeS_4,[48] Sn-*s* and S-*p* in Cu_2TSnS_4 (M = Mn and Fe),[50] and Co-*d* and S-*p* in Cu_2CoSnS_4.[52]

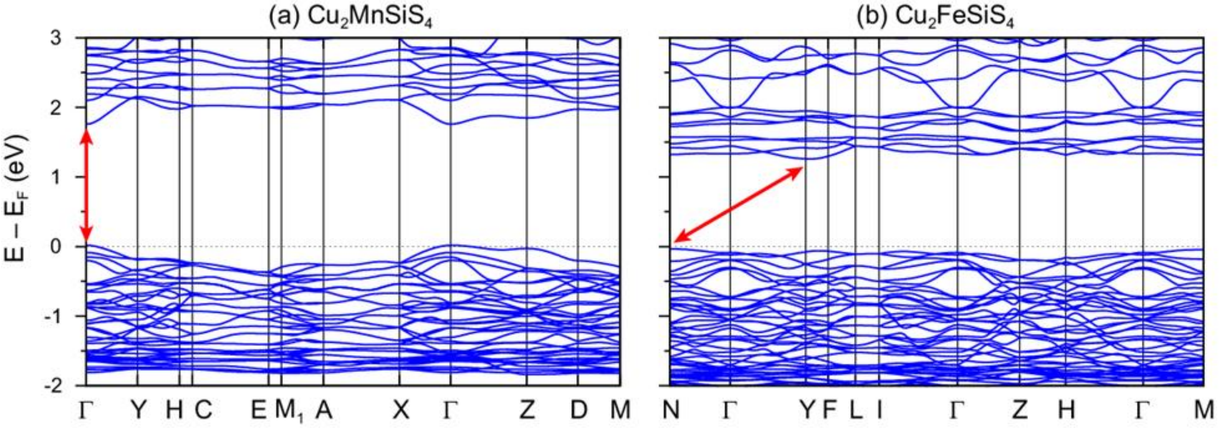

Figure 13. Band dispersions of Cu_2MnSiS_4 (a) and Cu_2FeSiS_4 (b) with collinear AFM structures.

The DFT calculations indicate that ordered magnetic moments are only realized in Mn (Fe) sites for Cu_2MnSiS_4 (Cu_2FeSiS_4). The size of the ordered magnetic moment is 4.55 μ_B/Mn and 4.35 μ_B/Fe for Cu_2MnSiS_4 and Cu_2FeSiS_4, respectively. Band structure calculations indicate that Cu_2MnSiS_4 is a semiconductor with a direct bandgap (E_g^{direct} =1.73 eV) located at Γ, while Cu_2FeSiS_4 is an indirect bandgap ($E_g^{indirect}$ = 1.52 eV) formed from N (VBM) to Y (CBM) (Figure 13). The calculated bandgaps are in a reasonable range compared to those calculated for the previously reported CTMS and related compounds: Ag_2FeSiS_4 (E_g^{direct} =1.99 eV),[53] Cu_2MnGeS_4 (E_g^{direct} = 1.72 eV),[48] Cu_2FeGeS_4 (E_g^{direct} = 1.8 eV),[54] Cu_2CoGeS_4 (E_g^{direct} = 0.81 eV),[51] Cu_2NiGeS_4 (E_g^{direct} = 1.76, 1.78 eV),[49] Cu_2MnSnS_4 (E_g^{direct} = 1.4, 1.52 eV),[50,55] Cu_2FeSnS_4 (E_g^{direct} = 1.7 eV),[50] Cu_2CoSnS_4 (E_g^{direct} = 1.2 eV),[52] and Cu_2NiSnS_4 (E_g^{direct} =1.29 eV).[50] The indirect bandgap is already reported in Ag_2MnSnS_4 ($E_g^{indirect}$ = 2.00 eV) and Li_2FeSnS_4 ($E_g^{indirect}$ = 1.42 eV) based on optical measurements.[56,42]

Conclusions

Both polycrystalline and single crystal Cu_2TSiS_4 (T = Mn and Fe) have been successfully prepared and adopt the same WSt polar crystal structure, supported by NPD, X-ray powder, and single crystal diffraction, TEM, and SHG measurements. The polar crystal structure also remains below 100 K based on temperature-dependent NPD experiments. Although Cu_2TSiS_4 (T = Mn and Fe) adopt the same crystal structure and show similar AFM behavior at low temperatures, their magnetic structures are distinct, with different magnetic propagation vectors. Interestingly, both magnetic Mn and Fe spins are canted away from the *ac* plane by about the same degree. Cu_2TSiS_4 (T = Mn and Fe) also show SHG responses, which fall in the same realm as related compounds, but both compounds are not PM in the region where they perform best. DFT calculations suggest the direct bandgap for Cu_2MnSiS_4 and the indirect bandgap for Cu_2FeSiS_4. As members of CTMS, Cu_2TSiS_4 (T = Mn and Fe) compounds are polar magnetic semiconductors with NLO response as well, which is rare in this series. The detailed study of polar crystal structure, magnetic structure, electronic structure, optical bandgaps, optical transparency in the IR region, and NLO responses will benefit the investigation of the large family of $AB^{II}M^{IV}X_4$ (A = alkali metals, Cu, and Ag; B = alkaline earth metals, transitional metals, Pb, and Eu; M = Si, Ge, and Sn; X = O, S, Se, and Te) compounds as multifunctional magnetic semiconductors with potential applications in photovoltaic, NLO, ferroelectric, magnetoelectric, and multiferroic areas.

ASSOCIATED CONTENT

Supporting Information. X-ray single crystal data collection and structure refinement parameters of Cu_2TSiS_4 (T = Mn and Fe); XRPD patterns of Cu_2TSiS_4 (T = Mn and Fe); electron diffraction of Cu_2MnSiS_4; EDX elemental maps and SEM image of a Cu_2FeSiS_4 single crystal; NPD patterns of Cu_2MnSiS_4 at 90 and 2 K and Cu_2FeSiS_4 at 100 and 2 K; Fourier transform infrared, attenuated total reflectance data plotted as percent transmittance for Cu_2TSiS_4 (T = Mn and Fe).

Accession Codes. CCDC numbers 2211730 and 2211728 contain the supplementary crystallographic data for Cu_2MnSiS_4 and Cu_2FeSiS_4, respectively. These data can be obtained free of charge from FIZ Karlsruhe via www.ccdc.cam.ac.uk/structures or by emailing data_request@ccdc.cam.ac.uk, or by contacting The Cambridge Crystallographic Data Centre, 12 Union Road, Cambridge CB2 1EZ, UK; fax: +44 1223 336033.

AUTHOR INFORMATION

Corresponding Authors* Email: jjcoupling@sogang.ac.kr, xtan6@gmu.edu

ACKNOWLEDGMENTS

Z. T. M. and X. T. were supported by start-up funding from George Mason University. J.A.A. and A.J.C. recognize funding provided by the United States National Science Foundation, DMR-1611198. J.I.J. acknowledges support from the Basic Science Research Programs (2021R1A2C2013625) through the National Research Foundation of Korea (NRF), funded by the Korean government. Special thanks to G&H Cleveland for donating the optical-grade AGS and AGSe reference materials that were used for NLO studies. N.J.G acknowledges the support from the National Science Foundation (NSF) CAREER award DMR-2143903. Magnetic measurements were supported by the U.S. Department of Energy, Office of Science, Basic Energy Sciences, Materials Science and Engineering Division. C.-J.K. was supported by the NRF grant (NRF-2022R1C1C1008200). This work used resources at the Spallation Neutron Source, DOE Office of Science Facilities operated by the Oak Ridge National Laboratory. TEM work was performed at the National High Magnetic Field Laboratory, which is supported by National Science Foundation Cooperative Agreement *No. DMR-1644779* and the State of Florida. We thank Dr. Thomas J. Emge (Rutgers, The State University of New Jersey) for helping with single crystal refinements.

REFERENCES

(1) Glenn, J. R.; Cho, J. Bin; Wang, Y.; Craig, A. J.; Zhang, J. H.; Cribbs, M.; Stoyko, S. S.; Rosello, K. E.; Barton, C.; Bonnoni, A.; et al. $Cu_4MnGe_2S_7$ and Cu_2MnGeS_4: Two Polar Thiogermanates Exhibiting

Second Harmonic Generation in the Infrared and Structures Derived from Hexagonal Diamond. *Dalt. Trans.* **2021**, *50*, 17524–17537.

(2) Wang, W.; Winkler, M. T.; Gunawan, O.; Gokmen, T.; Todorov, T. K.; Zhu, Y.; Mitzi, D. B. Device Characteristics of CZTSSe Thin-Film Solar Cells with 12.6% Efficiency. *Adv. Energy Mater.* **2014**, *4*, 1301465.

(3) Baskaran, P.; Nisha, K. D.; Harish, S.; Prabakaran, S.; Navaneethan, M.; Archana, J.; Ponnusamy, S.; Muthamizhchelvan, C.; Ikeda, H. High-Performance Electrocatalytic and Cationic Substitution in Cu_2ZnSnS_4 as a Low-Cost Counter Electrode for Pt-Free Dye-Sensitized Solar Cells. *J. Mater. Sci.* **2021**, *56*, 4135–4150.

(4) Sabry, N.; Zahran, H. Y.; Yousef, E. S.; Algarni, H.; Umar, A.; Albargi, H. B.; Yahia, I. S. Gamma-Ray Attenuation, Fast Neutron Removal Cross-Section and Build up Factor of $Cu_2MnGe[S, Se, Te]_4$ Semiconductor Compounds: Novel Approach. *Radiat. Phys. Chem.* **2021**, *179*, 109248.

(5) Isacfranklin, M.; Yuvakkumar, R.; Ravi, G.; Velauthapillai, D.; Pannipara, M.; Al-Sehemi, A. G. Superior Supercapacitive Performance of Cu_2MnSnS_4 asymmetric Devices. *Nanoscale Adv.* **2021**, *3*, 486–498.

(6) Ammar, H. R.; Sivasankaran, S.; Alaboodi, A. S.; Alshataif, Y. A.; Al-Mufadi, F. A. Synthesis, Phase Evolutions, Microstructures, and Compaction Behavior of Four Copper-Chalcogenide Micron-Thermoelectric Powders (Cu_2ZnSnS_4/Se_4, Cu_2MnSiS_4/Se_4, Cu_2MnSnS_4/Se_4, and Cu_2ZnSiS_4/Se_4) Prepared by Mechanical Alloying. *Mater. Chem. Phys.* **2021**, *271*, 124943.

(7) Xiao, C.; Li, K.; Zhang, J.; Tong, W.; Liu, Y.; Li, Z.; Huang, P.; Pan, B.; Su, H.; Xie, Y. Magnetic Ions in Wide Band Gap Semiconductor Nanocrystals for Optimized Thermoelectric Properties. *Mater. Horizons* **2014**, *1*, 81–86.

(8) Goto, Y.; Naito, F.; Sato, R.; Yoshiyasu, K.; Itoh, T.; Kamihara, Y.; Matoba, M. Enhanced Thermoelectric Figure of Merit in Stannite − Kuramite Solid Solutions Cu^{2+}. *Inorg. Chem.* **2013**, *52*, 9861–9866.

(9) Brockway, L. O. The Crystal Structure of Stannite, Cu_2FeSnS_4. *Zeitschrift fuer Krist. Krist. Krist. Krist.* **1934**, *89*, 434–441.

(10) Hall, S. R.; Szymanski, J. T.; Stewart, J. M. Kesterite, $Cu_2(Zn, Fe)SnS_4$, and Stannite, $Cu_2(Fe, Zn)SnS_4$, Structurally Similar but Distinct Minerals. *Can. Mineral.* **1978**, *16*, 131–137.

(11) Llanos, J.;Tapia, M.;Mujica, C.; Oro-Sole, J.; Gomez-Romero, P. A New Structural Modification of Stannite. *Bol. la Soc. Chil. Quim.* **2000**, *45*, 605–609.

(12) Schaefer, W.; Nitsche, R. Tetrahedral Quaternary Chalcogenides of the Type Cu_2-II-IV-$S_4(Se_4)$. *Mater. Res. Bull.* **1974**, *9*, 645–654.

(13) Allemand, J.; Wintenberger, M. Neutron-Diffraction Study of the Magnetic Structures of Cu_2MnSnS_4 and Cu_2MnGeS_4. *Cristallogr. Bull. la Soc. Fr. Mineral.* **1970**, *93*, 141–145.

(14) Nénert, G.; Palstra, T. T. M. Magnetoelectric and Multiferroic Properties of Ternary Copper Chalcogenides $Cu_2M^{II}M^{IV}S_4$. *J. Phys. Condens. Matter* **2009**, *21*, 176002.

(15) Bernert, Thomas; Pfitzner, A. $Cu_2MnM^{IV}S_4$ (M^{IV} = Si, Ge, Sn) - Analysis of Crystal Structures and Tetrahedral Volumes of Normal Tetrahedral Compounds. *Zeitschrift fuer Krist.* **2005**, *220*, 968–972.

(16) Quintero, M.; Quintero, E.; Moreno, E.; Marquina, J.; Alvarez, S.; Rincón, C. Magnetic Susceptibility for the Cu_2-II-IV-S_4 (II = Mn , Fe ; IV = Si , Ge or Sn) Compounds: Exchange Interaction Parameters of Ge and Sn. *Rev. Lat. Met. Mat.* **2017**, *37*, 27–34.

(17) Kirkham, M.; Heroux, L.; Ruiz-Rodriguez, M.; Huq, A. AGES: Automated Gas Environment System for *in Situ* Neutron Powder Diffraction. *Rev. Sci. Instrum.* **2018**, *89*, 092904.

(18) Rodríguez-Carvajal, J. Recent Advances in Magnetic Structure Determination by Neutron Powder Diffraction. *Phys. B: Condens. Matter* **1993**, *192*, 55–69.

(19) Perez-Mato, J. M.; Gallego, S. V.; Tasci, E. S.; Elcoro, L.; De La Flor, G.; Aroyo, M. I. Symmetry-Based Computational Tools for Magnetic Crystallography. *Annu. Rev. Mater. Res.* **2015**, *45*, 217–248.

(20) Sheldrick, G. M. A Short History of SHELX. *Acta Crystallogr. Sect. A Found. Crystallogr.* **2008**, *64*, 112–122.

(21) Mcgowan, R. J. Attenuated Total Reflectance vs. Transmission Infrared Spectrometry in the Quantitative Evaluation of Paint Vehicles. *Anal. Chem.* **1963**, *35*, 1664–1665.

(22) Zhang, J. H.; Clark, D. J.; Brant, J. A.; Rosmus, K. A.; Grima, P.; Lekse, J. W.; Jang, J. I.; Aitken, J. A. A-Li_2ZnGeS_4: A Wide-Bandgap Diamond-like Semiconductor with Excellent Balance between Laser-Induced Damage Threshold and Second Harmonic Generation Response. *Chem. Mater.* **2020**, *32*, 8947–8955.

(23) Blaha, P.; Schwarz, K.; Tran, F.; Laskowski, R.; Madsen, G. K. H.; Marks, L. D. WIEN2k: An APW+lo Program for Calculating the Properties of Solids. *J. Chem. Phys.* **2020**, *152*, 074101.

(24) Perdew, J. P.; Burke, K.; Ernzerhof, M. Generalized Gradient Approximation Made Simple. *Phys. Rev. Lett.* **1996**, *77*, 3865–3868.

(25) Anisimov, V. I.; Solovyev, I. V.; Korotin, M. A.; Czyyk, M. T.; Sawatzky, G. A. Density-Functional Theory and NiO Photoemission Spectra. *Phys. Rev. B* **1993**, *48*, 16929–16934.

(26) Anisimov, V. I.; Aryasetiawan, F.; Lichtenstein, A. I. First-Principles Calculations of the Electronic Structure and Spectra of Strongly Correlated Systems: The LDA + U Method. *J. Phys. Condens. Matter* **1997**, *9*, 767–808.

(27) Biniskos, N.; Dos Santos, F. J.; Schmalzl, K.; Raymond, S.; Dos Santos Dias, M.; Persson, J.; Marzari, N.; Blügel, S.; Lounis, S.; Brückel, T. Complex Magnetic Structure and Spin Waves of the Noncollinear Antiferromagnet Mn_5Si_3. *Phys. Rev. B* **2022**, *105*, 104404.

(28) Shannon, R. D. Revised Effective Ionic Radii and Systematic Studies of Interatomic Distances in Halides and Chalcogenides. *Acta Cryst.* **1976**, *A32*, 751–767.

(29) Guen, L.; Glaunsinger, W. S. Electrical, Magnetic, and EPR Studies of the Quaternary Chalcogenides $Cu_2A^{II}B^{IV}X_4$ Prepared by Iodine Transport. *J. Solid State Chem.* **1980**, *35*, 10–21.

(30) Gulay, L. D.; Nazarchuk, O. P.; Olekseyuk, I. D. Crystal Structures of the Compounds $Cu_2CoSi(Ge, Sn)S_4$ and $Cu_2CoGe(Sn)Se_4$. *J. Alloys Compd.* **2004**, *377*, 306–311.

(31) Chourio, M.; Romero, H.; Betancourt, L.; Sagredo, V. Crystal Growth and Magnetic Properties of the Cu_2MnGeS_4 Semiconductor. *New Trends Magn., Magn. Mater., Their Appl.* **1994**, *2*, 359–363.

(32) Shapira, Y.; McNiff, E. J.; Oliveira, N. F.; Honig, E. D.; Dwight, K.; Wold, A. Magnetic Properties of $Cu_2Zn_{1-x}Mn_xGeS_4$: Antiferromagnetic Interactions in the Wurtz-Stannite Structure. *Phys. Rev. B* **1988**, *37*, 411–418.

(33) Wintenberger, M. Study of the Crystallographic and Magnetic Structure of Dicopper(I) Iron(II) Germanium Sulfide (Cu_2FeGeS_4) and Comment on the Magnetic Structure of Dicopper(I) Manganese(II) Tin(IV) Sulfide (Cu_2MnSnS_4). *Mater. Res. Bull.* **1979**, *14*, 1195–1202.

(34) Delgado, G. E.; Sagredo, V. Synthesis and Crystal Structure of the Quaternary Semiconductor Cu_2NiGeS_4, a New Stannite-Type Compound. *Rev. Mex. Fis.* **2019**, *65*, 355–359.

(35) Beraich, M.; Shaili, H.; Benhsina, E.; Hafidi, Z.; Taibi, M.; Bentiss, F.; Guenbour, A.; Bellaouchou, A.; Mzerd, A.; Zarrouk, A.; Fahoume, M. Experimental and Theoretical Study of New Kesterite Cu_2NiGeS_4 Thin Film Synthesized via Spray Ultrasonic Technic. *Appl. Surf. Sci.* **2020**, *527*, 146800.

(36) Fries, T.; Shapira, Y.; Palacio, F.; Morón, M. C. Magnetic Ordering of the Antiferromagnet from Magnetization and Neutron-Scattering Measurements. *Phys. Rev. B - Condens. Matter Mater. Phys.* **1997**, *56*, 5424–5431.

(37) Allemand, J.; Wintenberger, M. Structural and Magnetic Properties of Some Stannite-Type Compounds. *Bull. la Soc. Fr. Mineral. Cristallogr.* **1970**, *93*, 14–17.

(38) Caneschi, A.; Cipriani, C.; Di Benedetto, F.; Sessoli, R. Characterisation of the Antiferromagnetic Transition of Cu_2FeSnS_4, the Synthetic Analogue of Stannite. *Phys. Chem. Miner.* **2004**, *31*, 190–193.

(39) Ganiel, U.; Hermon, E.; Shtrikman, S. Studies of Magnetic Ordering in Cu_2FeSnS_4 by Moessbauer Spectroscopy. *J. Phys. Chem. Solids* **1972**, *33*, 1873–1878.

(40) Bernardini, G. P.; Borrini, D.; Caneschi, A.; Benedetto, F. Di; Gatteschi, D.; Ristori, S.; Romanelli, M. EPR and SQUID Magnetometry Study of Cu_2FeSnS_4 (Stannite). *Phys. Chem. Miner.* **2000**, *27*, 453–461.

(41) Rincon, C.; Quintero, M.; Moreno, E.; Power, Ch.; Quintero, E.; Henao, J. A.; Macias, M. A.; Delgado, G. E.; Tovar, R.; Morocoima, M. X-Ray Diffraction, Raman Spectrum and Magnetic Susceptibility of the Magnetic Semiconductor Cu_2FeSnS_4. *Solid State Commun.* **2011**, *151*, 947–951.

(42) Brant, J. A.; Dela Cruz, C.; Yao, J.; Douvalis, A. P.; Bakas, T.; Sorescu, M.; Aitken, J. A. Field-Induced Spin-Flop in Antiferromagnetic Semiconductors with Commensurate and Incommensurate Magnetic Structures: Li_2FeGeS_4 (LIGS) and Li_2FeSnS_4 (LITS). *Inorg. Chem.* **2014**, *53*, 12265–12274.

(43) Kurtz, S. K.; Perry, T. T. A Powder Technique for the Evaluation of Nonlinear Optical Materials. *IEEE J. Quantum Electron.* **1968**, *39*, 3798–3813.

(44) Ohmer, Melvin C.; Pandey, R. Emergence of Chalcopyrites as Nonlinear Optical Materials. *MRS Bull.* **1998**, *23*, 16–22.

(45) Jackson, A. G.; Ohmer, M. C.; LeClair, S. R. Relationship of the Second Order Nonlinear Optical Coefficient to Energy Gap in Inorganic Non-Centrosymmetric Crystals. *Infrared Phys. Technol.* **1997**, *38*, 233–244.

(46) Fukushima, T.; Yamauchi, K.; Picozzi, S. Magnetically Induced Ferroelectricity in Cu_2MnSnS_4 and $Cu_2MnSnSe_4$. *Phys. Rev. B - Condens. Matter Mater. Phys.* **2010**, *82*, 014102.

(47) Zhu, Lin; Li, Lin; Cheng, T.-M. First Principle Study of the Electrochemical Properties of Li_2FeSiS_4. *Comput. Mater. Sci.* **2015**, *106*, 135–139.

(48) Beraich, M.; Shaili, H.; Hafidi, Z.; Benhsina, E.; Majdoubi, H.; Taibi, M.; Guenbour, A.; Bellaouchou, A.; Mzerd, A.; Bentiss, F.; Zarrouk, A.; Fahoume, M. Facile Synthesis of the Wurtz Stannite (Orthorhombic) Cu2MnGeS4 Thin Film via Spray Ultrasonic Method: Structural, Raman, Optical and Electronic Study. *J. Alloys Compd.* **2020**, *845*, 156216.

(49) El Hamdaoui, J.; El-Yadri, M.; Lakaal, K.; Kria, M.; Courel, M.; Ojeda, M.; Perez, L. M.; Laroze, D.; Feddi, E. Ab Initio Study on Electronic and Optical Properties of Cu_2NiGeS_4 for Photovoltaic Applications. *Sol. Energy* **2022**, *237*, 333–339.

(50) Chen, R.; Persson, C. Electronic and Optical Properties of Cu_2XSnS_4 (X = Be, Mg, Ca, Mn, Fe, and Ni) and the Impact of Native Defect Pairs. *J. Appl. Phys.* **2017**, *121*, 203104.

(51) Bourges, Cedric; Al Rahal Al Orabi, Rabih; Miyazaki, Y. Off-Stoichiometry Effect on Thermoelectric Properties of the New p-Type Sulfides Compounds Cu_2CoGeS_4. *J. Alloys Compd.* **2020**, *826*, 154240.

(52) Zhang, D.; Yang, J.; Jiang, Q.; Zhou, Z.; Li, X.; Xin, J.; Basit, A.; Ren, Y.; He, X. Multi-Cations Compound Cu_2CoSnS_4: DFT Calculating, Band Engineering and Thermoelectric Performance Regulation. *Nano Energy* **2017**, *36*, 156–165.

(53) Azam, Sikander; Khan, Saleem Ayaz; Goumri-Said, S. DFT Study of Optoelectronic and Magnetic Properties of Iron-Containing Diamond-like Materials Ag_2FeSiS_4, Li_2FeSnS_4, and Li_2FeGeS_4. *Solid State Sci.* **2017**, *72*, 71–79.

(54) Beraich, M.; Shaili, H.; Benhsina, E.; Hafidi, Z.; Mansouri, S.; Taibi, M.; Bentiss, F.; Guenbour, A.; Bellaouchou, A.; Mzerd, A.; Zarrouk, A.; Fahoume, M. Preparation and Characterization of Cu_2FeGeS_4 Thin-Film Synthesized via Spray Ultrasonic Method - DFT Study. *Mater. Lett.* **2020**, *275*, 128070.

(55) Rudisch, K.; Espinosa-Garcia, W. F.; Osorio-Guillen, J. M.; Araujo, C. M.; Platzer-Bjoerkman, C.; Scragg, J. J. S. Structural and Electronic Properties of Cu_2MnSnS_4 from Experiment. *Phys. Status Solidi B* **2019**, *256*, 1800743.

(56) Friedrich, D.; Greil, S.; Block, T.; Heletta, L.; Pöttgen, R.; Pfitzner, A. Synthesis and Characterization of Ag_2MnSnS_4, a New Diamond-like Semiconductor. *Zeitschrift fur Anorg. und Allg. Chemie* **2018**, *644* , 1707–1714.

For Table of Contents Only

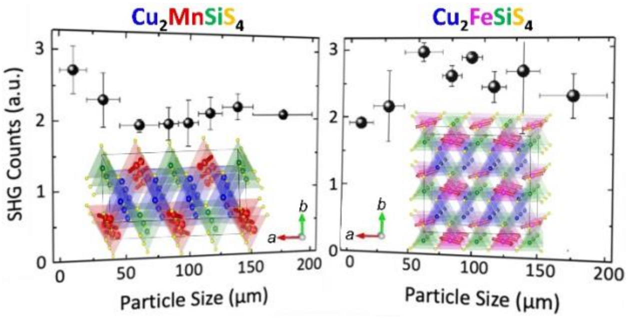

Isostructural polar semiconducting Cu_2MnSiS_4 and Cu_2FeSiS_4 show similar magnetic behavior and second harmonic generation response but display different magnetic structures with magnetic propagation vectors *k* = (½,0,½) and *k* = (½,½,½) for Cu_2MnSiS_4 and Cu_2FeSiS_4, respectively.